Physics of Fluids ARTICLE pubs.aip.org/aip/pof

Flow structure and dynamics behind cylinder arrays at Reynolds number ~100

Cite as: Phys. Fluids **35**, 067125 (2023); doi: 10.1063/5.0155102
Submitted: 18 April 2023 · Accepted: 5 June 2023 ·
Published Online: 22 June 2023

View Online Export Citation CrossMark

M. Sharifi Ghazijahani[1,a] and C. Cierpka[1,2]

AFFILIATIONS

[1]Institute of Thermodynamics and Fluid Mechanics, Technische Universität Ilmenau, 98684 Ilmenau, Germany
[2]Visiting research fellow, Department of Biomedical Engineering, Lund University, 22100 Lund, Sweden

[a)]Author to whom correspondence should be addressed: mohammad.sharifi-ghazijahani@tu-ilmenau.de

ABSTRACT

The flow behind nine different arrays of cylinders is experimentally investigated via Particle Image Velocimetry (PIV) at a Reynolds number of Re $\sim$100 based on the diameter of the cylinders. Each array consists of a column of four cylinders in front and three in the rear. The horizontal distance between the two columns and the vertical distance between the cylinders within each column are varied for $H/D = [2, 4, 8]$ and $V/D = [2, 4, 6]$, resulting in nine different arrays denoted as mVnH, where m corresponds to V/D and n stands for H/D. The PIV measurements are conducted for 15 s at 200 Hz frequency, corresponding to 39 to 360 vortex shedding events for the wakes in this study. Then, proper orthogonal decomposition is applied to the velocity fields to analyze the flow dynamics. All arrays show unsteady flow, and based on their flow structures, they are classified in to three main categories of single bluff body (SBB), transitional (TR), and co-shedding (CS) flow. SBB characteristics can be seen for 2V2H and 2V4H arrays, but the latter has more steady vortex shedding as the H/D increases from 2 to 4. Then, 2V8H and 4V2H have an asymmetric flow with several vortex streets and act as an intermediary stage in the shift from SBB to CS flow structure when the distances are increased. The highest total kinetic energy values and widest probability density functions of the velocity components are observed for this group. The five remaining arrays in the CS group have symmetric flow, with three or five vortex streets present behind. However, based on the distances, the frequency and phase synchronization of the vortex streets change considerably, which might have an important effect on, for example, the heat transfer or the structural load of the cylinders.

I. INTRODUCTION

Examples of flow past arrays of bluff bodies are widespread in nature and engineering. Offshore structures, marine risers, a group of chimney stacks, tubes in heat exchangers, bridge piers, wind farms, chemical reaction towers, and skyscrapers with close spacing are typical examples in engineering, while in nature, one can observe such structures in aquatic vegetation, close islands, or mountain chains. Even the sensing capacity of harbor seal vibrissae or whiskers can be modeled by this flow.[1–3] Aside from that, there are some attempts to harvest vibrational energy from such structures within flows through what is known as vortex-induced energy harvesting.[4–9]

When flow approaches an isolated cylinder, fluid viscosity results in the formation of a boundary layer around it; however, an adverse pressure gradient in the streamwise direction causes boundary layer separation on the rear side of the cylinder for large enough Re (well below 10), creating a highly turbulent region known as the wake. Eventually, the separated shear layer in the wake detaches from the up- and downsides of the cylinder in the form of discrete vortices, forming a vortex street with discrete vortex shedding frequency depending on the Reynolds number. This vortex street is known as von Kármán vortex street, and its effect on the flow structure, induced oscillations, and aerodynamic forces has been extensively studied. However, as already discussed in the previous paragraph, cylinders are present in the form of organized or random arrays in nature and engineering, and the introduction of further cylinders to the flow results in interaction between the boundary layers and vortex streets. Even the experienced upstream flow will change in the case of the presence of bodies upstream. This creates very rich and complex flow dynamics depending on the arrangement of the cylinders in the arrays.

In this regard, a more generic approach is to study the flow past patches of cylinders.[10–21] However, several categories of such arrays have been identified and studied in the last few years. Flow past multiple tandem cylinders has been studied to reveal the effect of the presence of bluff bodies upstream on the flow structure.[22–45,95–98]

For two cylinders, depending on the distance between the objects, there are three possible scenarios: extended-body flow, reattachment flow, and co-shedding flow.[23,46] When the pitch distance between the two objects is large enough, a two-row shear layer structure is formed and co-shedding flow is represented, whereas, for smaller distances, the frontal cylinder does not produce its independent vortex street. However, adding a third cylinder will result in a much larger complexity.[47]

For flow past two side-by-side cylinders, similar investigations have been carried out recently,[9,48–66] where authors reported five different flow regimes based on the cylinders' proximity L/D, where L is the distance between the cylinders and D, their diameter. Initially, for L/D < 1.2, there is no jet (gap) flow between the cylinders, and the entire set behaves like a single bluff body (SBB). Then, the flow pattern changes from a single bluff body flow to a deflected or flip-flopping pattern as the distance between the cylinders increases. Finally, for even more considerable distances of the cylinders, in-phase or anti-phase vortex shedding will happen based on the L/D. Additional flow characteristics, such as modulation and asymmetry, will occur around three cylinders side-by-side. In modulation, the central cylinder has a slightly higher vortex shedding frequency.[66,67]

For the staggered arrangements of two cylinders, the alignment angle with respect to free stream α, the distance L between cylinders, and their diameter D determine the flow regime.[68–72] This arrangement exhibits five different flow regimes: base bleeding, shear layer reattachment, vortex pairing and enveloping, vortex impingement, and complete vortex-shedding.[68] The interactions were described as boundary layer–cylinder, shear layer or wake cylinder, shear layer–shear layer, vortex cylinder, vortex–shear layer, and vortex–vortex.[70] A strong three-dimensionality of the flow was reported in the gap between the cylinders.[71]

Tandem, side-by-side, and staggered cylinders each have their own distinct characteristics and variations, but in reality, a combination of all are typically encountered. One of the most typical cylinder arrays is the three circular cylinders in equilateral–triangular arrangement (one placed upstream), which has been investigated by many in recent years, focusing on a specific feature of the flow.[73–78] Chen *et al.* simulated the flow structure for $Re = 50$–300 and $L/D = 1.0$–6.0,[79] and the oscillation regimes of vortex-induced vibrations for $Re = 100$ and $L/D = 2.0$–5.0,[80] where in the latter, the cylinders were elastically mounted. They concluded that L/D and Re have a significant influence on the hydrodynamics of the flow. Up to nine flow regimes are identified in the simulations. For $Re = 100$, single bluff-body flow ($L/D = 1.0$–1.4), deflected flow ($L/D = 1.5$–1.9), flip flopping flow ($L/D = 2.0$–2.5), anti-phase flow ($L/D = 2.6$–2.8 and 3.5–4.1), in phase flow ($L/D = 2.9$–3.4 and 4.2–4.5), and fully developed in-phase co-shedding flow ($L/D = 4.6$–6.0) were identified. Three additional wake patterns emerge when $Re = 50$–175 is considered, namely, steady symmetric flow, steady asymmetric flow, and hybrid flow. Similar to the flow structure, the oscillation regimes and underlying mechanisms of vortex-induced vibrations are significantly varied based on the flow structure, and five distinct regimes are observed there as well.

Two-dimensional numerical simulation of flow past six circular cylinders arranged in rectangular formation in two rows and three columns was conducted in $Re = 100$ by Gao *et al.*,[81] and four flow regimes are observed based on L/D: single bluff body, shielding, reattachment, and co-shedding flow. Sui *et al.*[8] investigated the output characteristics of different piezoelectric energy harvester arrays based on flow-induced vibration. Two and three cylinders in both tandem and side-by-side arrangement, and nine cylinders in square formation were studied. They found the highest average value of energy harvesting capacity and lowest initial vibrational velocity for the array of nine cylinders in square formation. Cornejo Maceda *et al.*[82] stabilized the flow past three rotating cylinders in triangular formation (fluidic pinball), with automated gradient-enriched machine learning algorithms. Some studies have also attempted flow modeling and control as well. Deng *et al.* was successful in the Galerkin force modeling[83] and cluster-based hierarchical network modeling of fluidic pinball.[84] Li *et al.*[85] implemented an exploratory gradient method for active drag reduction of fluidic pinball. The net drag power was reduced by 29% at $Re = 100$.

This study experimentally investigates the flow structure and dynamics of nine different arrays of seven cylinders. The cylinders are arranged in two columns, four cylinders in front, and three in the rear. Then, the horizontal distance between these two columns (H/D) and the vertical distance between the cylinders in the columns (V/D) is varied for $H/D = [2, 4, 8]$, and $V/D = [2, 4, 6]$. Thus, the arrays are kind of a combination of tandem, side-by-side, and staggered arrangement of cylinders, as mentioned above. The measurements are conducted via particle image velocimetry (PIV) for Re $\sim$100. The Re = 100 was chosen primarily since it is commonly used in the literature to describe flow around cylinder arrays. Therefore, comparing the results with previous studies for different configurations is easier and the dataset is complemented by this arrangement. From the fluid dynamical perspective, it is interesting as the flow for Re = 100 is already unsteady and very rich in dynamics. This is especially the case for the arrangement of multiple cylinders as one could also define a Reynolds number based on some characteristic dimension of the array, which then would be much higher. Thus, although higher Reynolds numbers will add extra information, general conclusions about the unsteady flow for these configurations are already possible. Flow structures are then described by analyzing the instantaneous and average velocity fields. Finally, proper orthogonal decomposition (POD) is applied to the data to analyze the long-term dynamics of the flow.

In this study, we have taken a step forward in understanding the flow behind cylinder arrays in the Reynolds number range similar to those of most studies (Re < 500). However, it differs from previous studies in that it is experimental and because the arrays are arranged in a new form that makes independent wake flows a possibility. Furthermore, while side-by-side, tandem, and staggered arrangements of cylinders have been investigated in the past and each represented its own distinct features, the zigzag arrangement of the arrays in the current study provides the possibility to investigate the combined effect of the three aforementioned arrangements, meanwhile that it is not truly identical to any of those. It is also expected that the interaction of the wake flows is maximized in this case, which would be beneficial for, e.g., heat transfer problems. It can even be argued that to some extent when $V/D = H/D$, the arrangements can also be referred to as the case where three equilateral–triangular cylinders are placed in a side-by-side arrangement in the flow. In addition, the long-time measurement of the flow allows further analysis of the unsteady flow behind such arrays.

II. EXPERIMENTAL SETUP

Figure 1 shows a schematic sketch of the experimental setup. Flow behind nine different cylinder arrays inside a water channel is measured via particle image velocimetry (PIV). Each array consists of seven cylinders arranged in two columns: four in the front and three in the rear. All cylinders are rigid and have a diameter of 1 mm. However, the horizontal distance between these two columns (H) and the vertical distance between cylinders inside each column (V) are varied for $H = [2, 4, 8]$ mm and $V = [2, 4, 6]$ mm. The water channel has a cross section of $50 \times 50\,\mathrm{mm}^2$. The flow was seeded by polyamide particles of $5\,\mu$ m in diameter and hallow glass spheres of $10\,\mu$ m in diameter, with the density of 1.03 and $1.1\,\mathrm{g/cm}^3$, respectively. The polyamide particles were used for the arrays with $V/D = 2$ and 4, whereas for the arrays with $V/D = 6$, larger tracer particles were needed to keep the high signal-to-noise ratio for the larger field of view, and thus, the hallow glass spheres with twice the diameter were used instead. The particle concentration was set to meet the criteria for good PIV data evaluation,[86] which states a minimum of six–ten particles per interrogation window size if no averaging is done.[87] The vertical mid-plane of the channel was illuminated by a continuous-wave laser (Laserworld Green-200 532). Optical elements formed a light sheet with a thickness of 1 mm. Then, a high-speed camera (HS 4M by LaVision GmbH) perpendicular to the laser sheet outside the channel captured PIV images of the illuminated particles. It was necessary to calibrate the images against a calibration target since the camera was close to the flow and there were no wall boundaries in the images. The target was two-dimensional, consisting of white dotes on a black background. The Reynolds number (Re) based on the diameter of the single cylinder (D) is $Re = V_\infty D/\nu \sim 100$. Here, V_∞ stands for free stream velocity ($V_\infty = 133$ mm/s) and ν is the kinematic viscosity. The free stream velocity in the case of no cylinder present in the flow is denoted as V_∞. It should be noted that for the test section of the channel, the flow is fully developed. The data were collected at 200 Hz recording frequencies with 15 s measurement durations. For the wakes in the current study, this corresponds to 39 to 360 vortex shedding events, which is long enough to achieve convergence in the data. Figure 2 shows the evolution of the mean value for the horizontal velocity u in time at a selected point in the middle of field of view for each array. The locations of the selected points are represented by small black crosses in Fig. 4. In about less than 9 s, the average values converge in all arrays. The latest convergence belongs to 4V2H array, which is in line with its extremely asymmetric and unsteady flow structure as later will be discussed. Although the evolution of the mean values for the vertical velocity v is not shown here, similar trends are observed for them with even faster convergence.

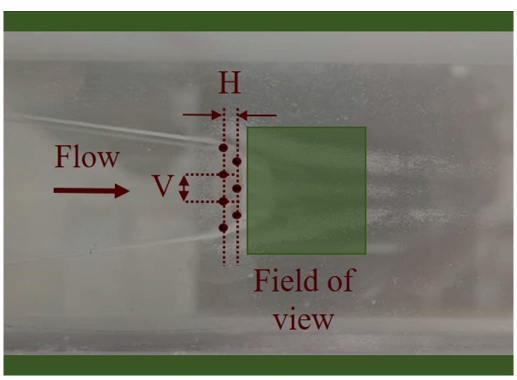

FIG. 1. Photograph of the field of view for the PIV measurements and the arrangement of the cylinders in the flow. In total, there are nine different sets of cylinders, with $V = [2, 4, 6]$ mm and $H = [2, 4, 8]$ mm.

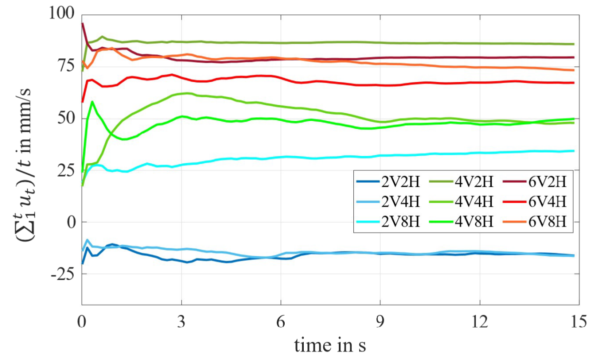

FIG. 2. The evolution of the mean value for the horizontal velocity u over time at the middle of the field of view for each array.

The PIV processing was performed using an advanced cross-correlation evaluation via DaVis 10 software (LaVision GmbH) for an initial rectangular interrogation window size of 64×64 pixels with 50% overlap, and a final circular Gaussian window weighting of 16×16 pixels again with 50% overlap. The number of passes of the initial and final interrogation windows was two and three, respectively. For the arrays with $V = 2$ and 4 mm, the final spatial resolution was $0.069 \times 0.069\,\mathrm{mm}^2$, while for the arrays with $V = 6$ mm, the final spatial resolution was $0.12 \times 0.12\,\mathrm{mm}^2$ in physical coordinates. All arrays had 231×138 vectors. In a normalized median test, the number of outlier vectors is under two percent for all arrays.[88] The absolute error can be estimated to be 0.1 pixels in properly adjusted experiments.[89] The dynamic spatial and velocity ranges are [0–14] pixels and [0–150] mm/s, respectively. This results in minimum relative uncertainties of 1% and 1.3% for $V = 2$, 4 and $V = 6$ in the free stream. However, in areas with lower displacements, the values will be higher. Details about recent PIV algorithms, including the one used in the current study, can be found in Kähler *et al.*[90]

III. RESULTS

This section includes the presentation and analysis of the PIV measurement results. Furthermore, in order to better understand the flow dynamics, snapshot proper orthogonal decomposition[91] (POD) was applied to the data. Flows with complex geometry, especially wake flows, have long been analyzed using POD-based reduced-order models,[92,93] and here, POD will assist in analyzing the spatial and temporal distribution of the structures in the flow. From now on, the arrays will be referred to as mVnH where m and n represent the vertical (V/D) and horizontal (H/D) distances between the cylinders, respectively.

A. Classification

Figure 3 shows the average absolute velocity ($|V|$) magnitudes behind the arrays. Even though each array represents a distinct flow structure, as will be shown later, some general classifications of the

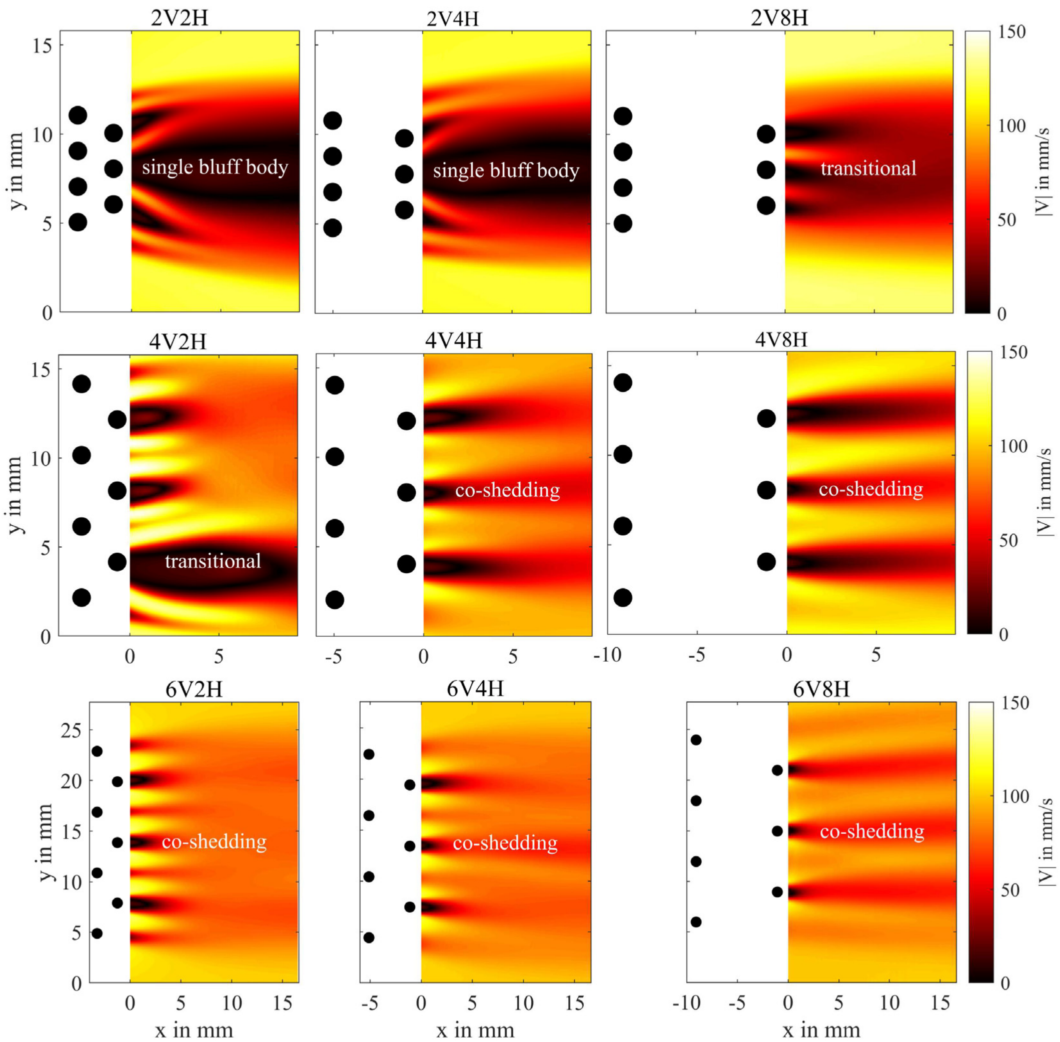

FIG. 3. Time-averaged absolute velocity ($|V|$) field behind the arrays. The free stream velocity is $V_\infty = 133$ mm/s.

flow structures can still be made from the average flows. The 2V2H and 2V4H arrays represent single bluff body flow. Meaning that due to the proximity of the cylinders, the flow sees the array as a single bluff body and there is a single large vortex street behind. Then, there are groups of five arrays, namely, 4V4H, 4V8H, 6V2H, 6V4H, and 6V8H, which represent co-shedding flow. This means that all the individual cylinders in the second column and some of the cylinders in the first column represent individual vortex streets. Finally, there is a third group of arrays, 2V8H and 4V2H, that have strongly asymmetric and irregular flow, and they appear to be the transition from single bluff body flow to co-shedding flow. While most arrays have ($|V|$) values equal or less than free stream velocity ($V_\infty = 133$ mm/s), 4V2H has even higher values up to 150 mm/s emerging from the gaps between cylinders.

In order to have a general overview about the fluctuations, Fig. 4 shows the Total Kinetic Energy (TKE) distribution behind each array. TKE is defined as

$$TKE = \Sigma_{t=1}^{T} \frac{(u_t - \bar{u})^2 + (v_t - \bar{v})^2}{2}. \tag{1}$$

This is important as any form of vibrational energy harvesting or heat transfer behind these arrays, or calculation of the vibrational load over the structures behind, requires an understanding of the TKE distribution and that high TKE is good for heat transfer but bad for structure load. While arrays of single bluff body flow (2V2H and 2V4H) represent a circle of high TKE values behind, and co-shedding arrays show symmetric stretched regions of high fluctuations behind the cylinders, the transitional group (2V8H and 4V2H) show very asymmetric patterns. Within all nine arrays, the highest and lowest TKE values are seen in 4V2H ($\approx 5 \times 10^6$ mm^2/s^2) and 2V2H ($\approx 5 \times 10^3$ mm^2/s^2) arrays, respectively. This indicates how significantly the flow structure can change by only increasing the vertical distance between the cylinders from 2D to 4D. For 4V8H, the minimum TKE values occur

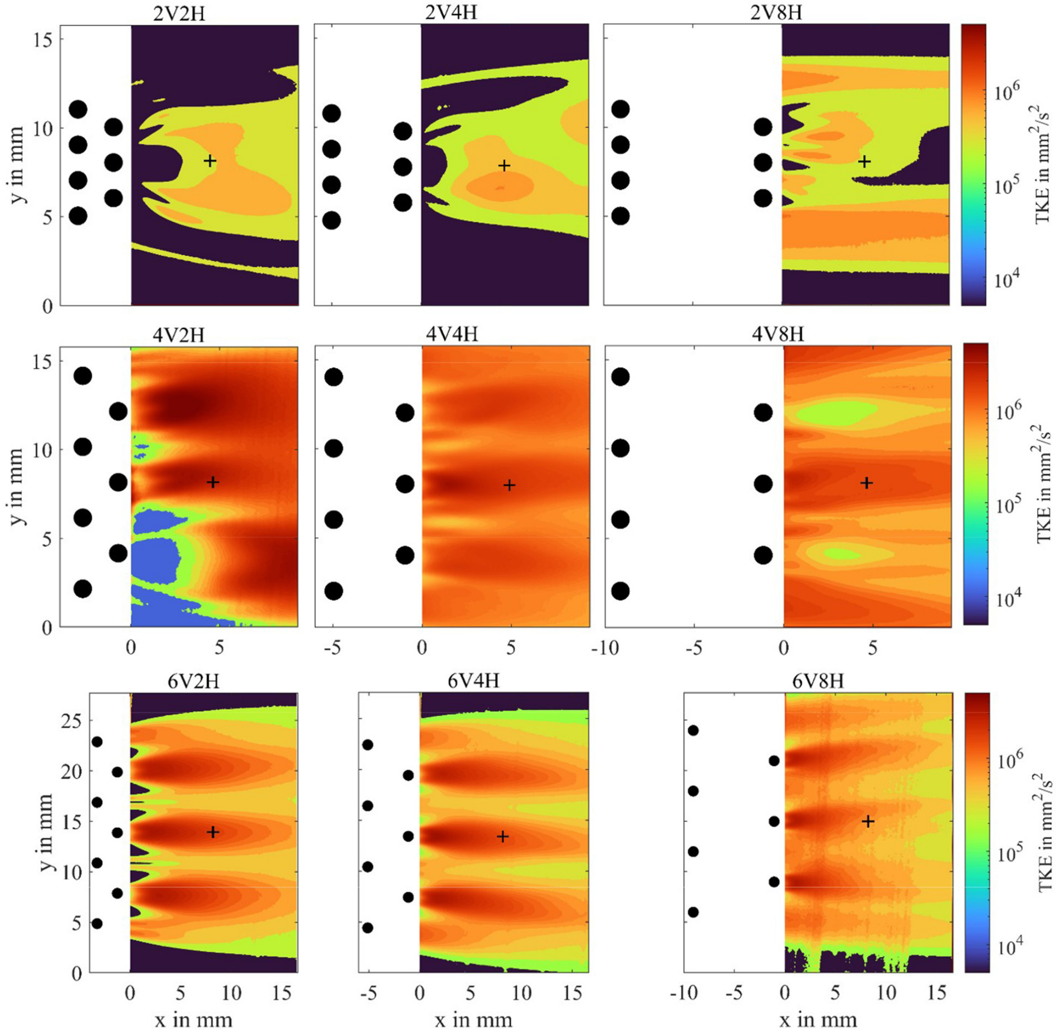

FIG. 4. Total kinetic energy (TKE) distribution behind the arrays. The black crosses at the center of each TKE field represent the coordinates of the points, which were used to show the evolution of the mean horizontal velocity u over time in Fig. 2.

behind the upper and lower cylinders in the second column, while the neighboring central cylinder represents the highest TKE values. The same is true for 4V4H to a lesser extent.

For further understating of the fluctuations behind the arrays, the probability density function (PDF) of the vertical (V_y) and horizontal (V_x) velocities is shown in Fig. 5. The PDF can be formulated as

$$PR_u(a < u < b) = \int_a^b PDF_u \, du. \tag{2}$$

Here, PR stands for the probability of values in the respective range of velocity. When the PDF distributions are compared, it should be considered that the size of the field of view is larger for the arrays with $V/D = 6$. In general, the 4V2H array has the widest PDF for both V_y and V_x. This is in line with what has been shown in TKE fields, where this array also had the most asymmetric extreme values of TKE. For V_y, the 2V2H array has two additional peaks other than $V_y = 0$. These two are basically the typical upward and downward velocity values inside its vortex street. For the 2V4H array, these two peaks are also almost visible, but they diminish and disappear as V/D and H/D increase. For the PDF profiles of V_x, there is a band of high probability V_x values for each array. For example, for 2V2H and 2V4H arrays, this band is stretched from almost $V_x = -10$ mm/s to $V_x = 130$ mm/s. While the 130 is the representation of the free stream in the flow, the -10 is where the flow turns back in the recirculation zone of the flow within the vortex street immediately after the object(s). This negative peak value is represented in all arrays. Therefore, the backward velocity magnitude in the recirculation zone is quite comparable between the different wake configurations.

The energy distributions of the POD modes are shown in Fig. 6. In principle, by comparing the energy distributions of the POD modes of the arrays, one can obtain a more general understanding of how comparatively complex the flow structure behind each array is. In this

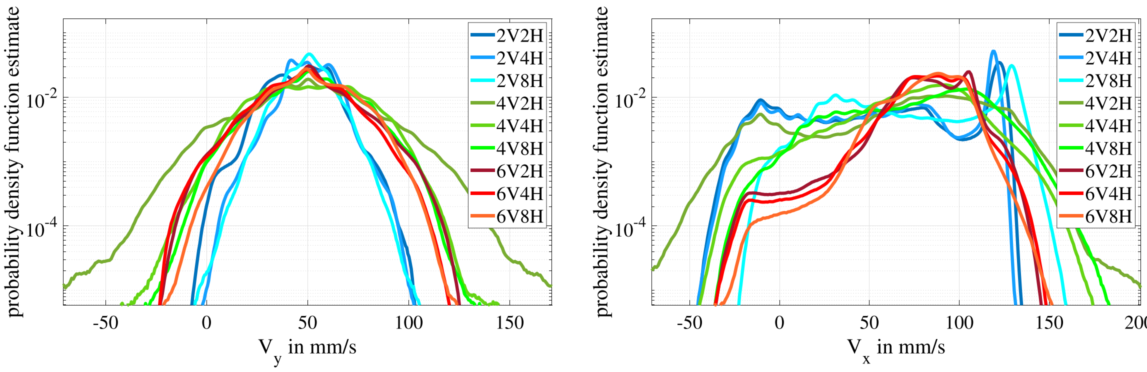

FIG. 5. Probability density function (PDF) of the vertical (left) and horizontal (right) velocity components for the arrays.

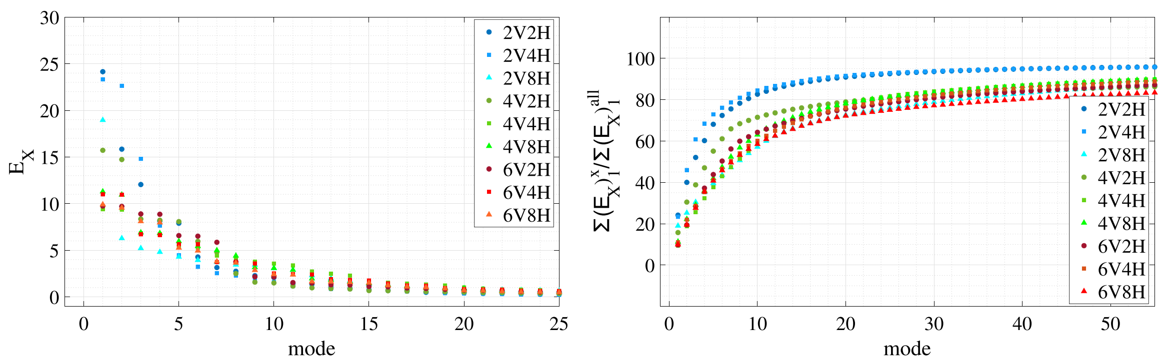

FIG. 6. Energy of POD modes for the arrays. Modal kinetic energy percentage (left) and sum of kinetic energy percentage (right).

regard, Fig. 6 right shows the sum of energies of the POD modes for each array. Comparatively, the flow structure becomes simpler as cumulative energy increases. Depending on the array, the first ten modes can account for 57% to 84% of the total kinetic energy. It is evident that there is a significant difference between the arrays in terms of flow complexity. The arrays can be classified into two groups and one intermediary based on their energy distributions. 2V2H and 2V4H have the simplest structures, while 4V2H is an intermediate, and others have quite similar degrees of complexity. The shares of each individual POD mode in the total kinetic energy are shown in Fig. 6 left. Basically, one can categorize the most energetic modes into two groups. One group for the modes representing the vortex shedding(s) in the flow and another group for the oscillations in the jet flows in the gaps between the cylinders and/or in the recirculation zones behind the cylinders. Table I shows a brief description of the flow structure behind each array. Furthermore, discussions will be continued in the next sections.

Finally, before deeper analyzing the flow behind individual arrays, general observations can be made about the jet flows emerging from the gaps between the cylinders. As can be seen in Fig. 3, all arrays show these jet flows in their average velocity fields. However, the magnitude, direction, and length vary significantly. As the vertical and

TABLE I. A brief description of the flow characteristics behind each array. *For 2V2H and 2V4H due to the single bluff body flow, the width of entire array set is considered for Strouhal number calculation.

Array	2V2H	2V4H	2V8H	4V2H	4V4H	4V8H	6V2H	6V4H	6V8H
Vortex shedding frequency in Hz and (Strouhal number)	2.6 (0.14)*	2.6 (0.14)*	18(0.13)	24(0.18)	16(0.12)	18(0.13)	18(0.13)	19(0.14)	15(0.11)
			...	13(0.10)	16(0.12)	...	14(0.11)	19(0.14)	15(0.11)
			...	18(0.13)	16(0.12)	18(0.13)	14(0.11)	19(0.14)	15(0.11)
			...	6(0.05)	16(0.12)	...	14(0.11)	19(0.14)	15(0.11)
			18(0.13)	...	16(0.12)	18(0.13)	18(0.13)	19(0.14)	15(0.11)
Energy percentage of top ten modes	83	84	57	71	59	63	64	60	58
Symmetric	Yes	Yes	No	No	Yes	Yes	Yes	Yes	Yes

horizontal distances increase, the angle between the jets and the free stream approaches zero. For a fixed V/D, the increase in H/D will result in more stretched jets that cover almost the entire field of view and prevent the vortex streets in between from colliding and mixing with neighboring wakes. For the power or magnitude of jet flows, there is not a general trend with respect to the increase in distances, and the highest values belong to the 4V2H array with velocity magnitudes even higher than the free stream velocity. Finally, both arrays with transitional flow structures (2V8H and 4V2H) have significantly asymmetric jet flows.

B. Single bluff body

Figure 7 shows the flow behind 2V2H and 2V4H arrays at the top and bottom, respectively. For each array, the instantaneous absolute velocity field, the spatial POD modes (SPM), and the respective time coefficients of POD modes (TCPM) are shown in left, middle, and right, respectively. In both arrays, the instantaneous velocity fields indicate a single bluff body flow with a large vortex street behind the arrays due to the extreme proximity of the cylinders. These vortex streets are shown in the second and third modes in 2V2H and the first and second modes in 2V4H. As evident from comparing these SPMs, the vortex shedding center has slightly moved upwards toward the cylinders in the 2V4H array. The TCPMs of the respective modes show a similar vortex shedding frequency of 2.6 Hz for both arrays; however, the vortex shedding is significantly unstable for the 2V2H. Based on the stream-wise cross-sectional length of the entire array (7D), the Reynolds number is $Re = 900$, which results in the Strouhal number of $St = fD/V_\infty = 0.14$.

The jet flows that originate from the gaps between the cylinders are another major feature of the flow behind these arrays. In the vicinity of the arrays, the main flow characteristics are these jet flows, as the vortex formation center downstream is relatively far away. Even though they appear symmetric in time-averaged fields (Fig. 3), instantaneous velocity fields indicate that their fluctuations are responsible for vortex shedding. For 2V4H, the jet flows are represented in the third mode with 15% of total kinetic energy (TOTKE), while for the 2V2H array, this appears in the first mode with 24% of TOTKE. Thus, although they have a similar shape in both arrays, for 2V2H, they appear to have more fluctuations. Considering the fact that 2V8H and 4V2H do not exhibit single bluff body flow, it can be concluded that the limit for having single bluff body (SBB) flow behind the arrays is certainly somewhere around $2 < V/D_{SBBmax} < 4$ and $4 < H/D_{SBBmax} < 8$.

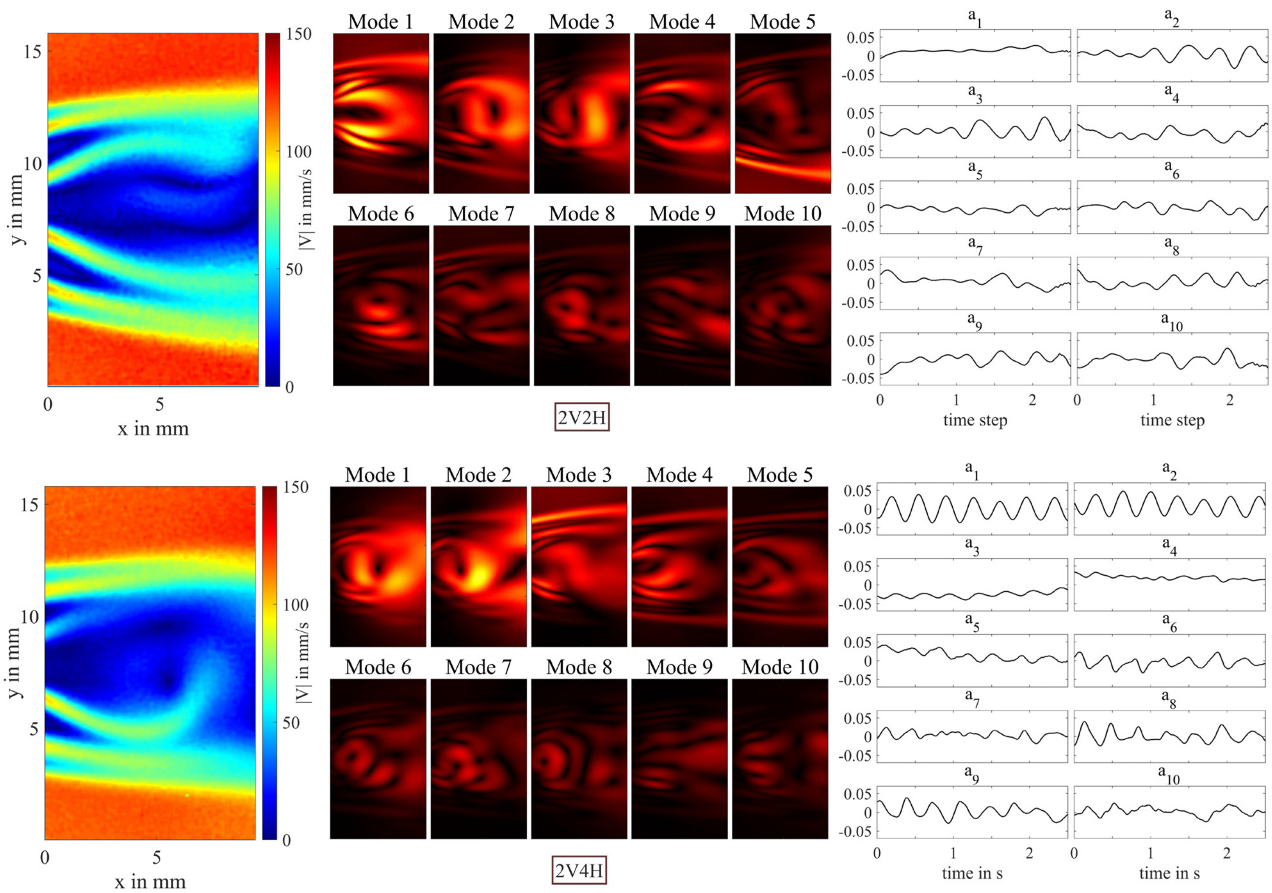

FIG. 7. The instantaneous absolute velocity field $|V|$ (left), the spatial POD modes (center), and their corresponding time coefficients (right) for the 2V2H and 2V4H arrays at top and bottom, respectively.

C. Transitional

As the distance between the cylinders further increases, the flow regime transforms from single bluff body to co-shedding flow. However, this transition is not immediate, and intermediary flow regimes appear in between. As already discussed in the classification section, the flow behind 2V8H and 4V2H arrays are classified as transitional flows. The results for the 2V8H array are shown at the top of Fig. 8. The flow regime has clearly shifted from a single bluff body flow in 2V2H and 2V4H. Three distinct tails as the recirculation zones behind the cylinders in the second column are visible. However, the average flow in Fig. 3 shows that the flow is asymmetric, with the upper cylinder in the second column having a longer tail than the lower ones. The SPM one represents the fluctuation in the tail of the lower cylinder in the second column, and its distinct kinetic energy of 19% (see Fig. 6) indicates significant perturbations in this region. This aligns with TKE values in Fig. 4, where they also reflect the high turbulence in this region. It should be noted that despite the tails fluctuating over time, the upper cylinder in the second column has a longer recirculation zone for almost the entire measurement period. Modes 3–4 and 7–8 correspond to the vortex streets of the upper and lower cylinders of the first column, respectively. There is no synchronization between them, as different modes correspond to these two vortex streets. As can also be seen from the instantaneous velocity fields, these two cylinders in the first column were the only ones able to shed distinct vortices due to their location at the edges. From their respective TCPMs, it is apparent that both have unsteady vortices with similar structures and frequencies of 18 Hz.

The results for the 4V2H array are shown in Fig. 8 bottom. There is a significant asymmetric flow behind the array due to a large recirculation zone (tail) behind the lower cylinder in the second column for its vortex street that sheds with 6 Hz frequency. This is by average at least three times longer than the tails of the other two cylinders in the second column. Even though its length fluctuates over time, this particular cylinder has the longest recirculation zone for the entire measurement time. Because of the considerable backward flow within this large recirculation zone, this array has the highest PDF values for negative V_x in Fig. 5 right. Furthermore, among all nine arrays of the study, it has the highest values for TKE (see Fig. 4), and depending on where an observer would be positioned behind the array, significantly different perturbations are faced. The large tail suppresses the vortex shedding of the lower cylinder in the first column. The central and upper cylinders in the second column and the upper one in the first column have vortex

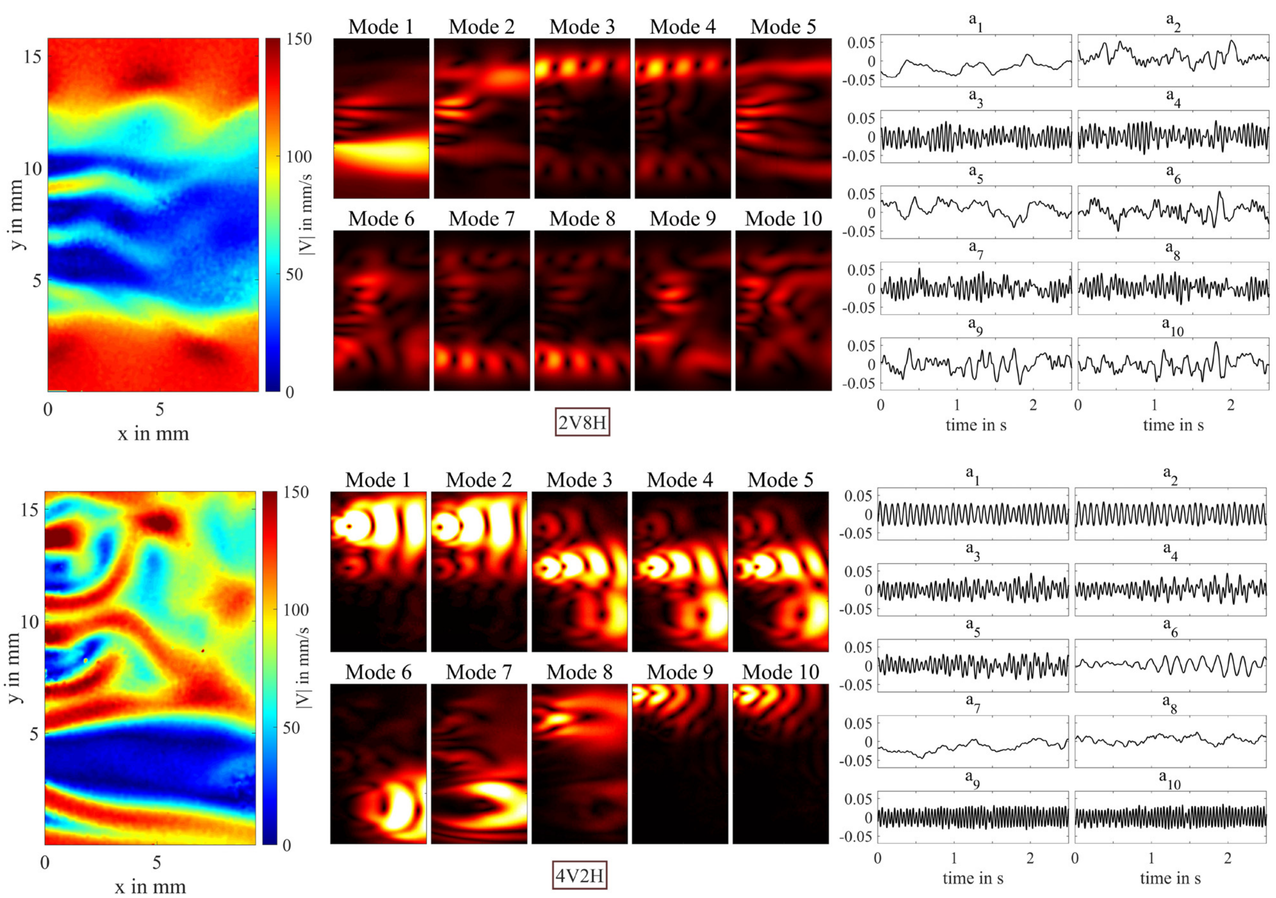

FIG. 8. The instantaneous absolute velocity field $|V|$ (left), the spatial POD modes (center), and their corresponding time coefficients (right) for the 2V8H and 4V2H arrays at top and bottom, respectively.

shedding frequencies of 18, 13, and 24 Hz, respectively. In the entire arrays, 24 is the highest observed frequency, even higher than a single isolated cylinder in a flow [$f = 22$ Hz (Ref. 94)]. The most energetic modes belong to the vortex street behind the upper cylinder in the second column, with almost 15% of TOTKE. It is also rather interesting that the central cylinder in the second column shows a higher frequency in the wake in comparison with its neighbors, and its vortex street is represented via three modes (3, 4, and 5) in the SPMs. Similarly to 2V8H, neither of the vortex streets in this array are synchronized.

Generally, for 2V8H and 4V2H, the distances between the cylinders are large enough to prevent the array from acting as a single bluff body in front of the flow. However, they are still not large enough to let each cylinder represent its own vortex street in a relatively symmetric way. Therefore, irregular and asymmetric flow patterns arise behind the arrays, which are not ideal in terms of the hydrodynamic or aerodynamic forces acting on the bodies inside the arrays or behind them downstream. However, it would definitively avoid resonances, since frequencies may change over time and space.

D. Co-shedding

As the distance between the cylinders further increases, the co-shedding flow appears behind the arrays. In this scenario, flow is symmetric on average (although some temporary asymmetric flows might emerge), and all the cylinders in the second column and the two upper and lower cylinders in the first column have their own distinct vortex streets (4V8H is an exception to this). However, the vortex streets are still clearly interacting with each other, and each of the five arrays in this group (4V4H, 4V8H, 6V2H, 6V4H, and 6V8H) has different flow structure and dynamics to some extent. For 4V4H (Fig. 9, top), the five vortex streets are shedding with 16 Hz frequency. The central cylinder in the second column has a smaller recirculation zone compared to its neighbors. However, it is considerably fluctuating, as shown in SPM 7. Thus, the TKE behind this cylinder is higher than the other two in the second column (Fig. 4).

The configuration 4V8H represents extended tails behind the two upper and lower cylinders in the second column (Fig. 9, bottom). Here, the fluctuations are small, and TKE values are the lowest (see the green area behind these two cylinders in Fig. 4). Although the two vortex streets of the upper and lower cylinders in the first column are apparent at the edges however, in the center, instead of a distinct vortex street, the entire area between the two elongated tails oscillates. All three have a frequency of 18 Hz; however, the oscillations at the center are synchronized with the lower vortex street. This is inferred from the fact that the first SPM pair captured the oscillations in these two streets

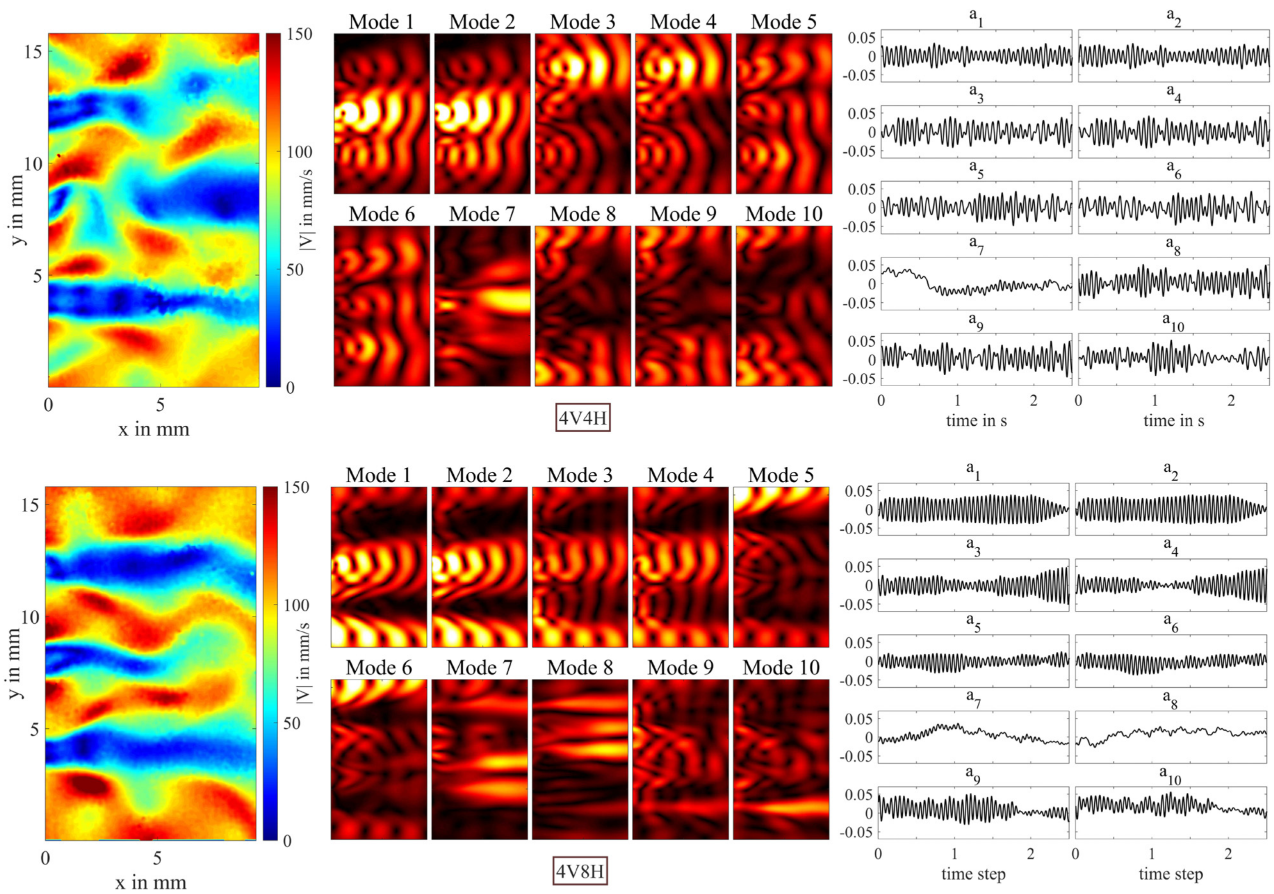

FIG. 9. The instantaneous absolute velocity field $|V|$ (left), the spatial POD modes (center), and their corresponding time coefficients (right) for the 4V4H and 4V8H arrays at top and bottom, respectively.

together, while the upper street has its own pair of SPMs representing its fluctuations.

As the V/D increases to 6, one might expect a minimal interaction between the flows behind the cylinders. Although by looking at the instantaneous velocity fields in Fig. 10, this might seem to be the case, however, the POD analysis proves the opposite. First, let's again remind that an individual cylinder for the current Reynolds number will have steady vortex shedding with 22 Hz frequency.[94] Second, one should consider that if there is any synchronization between the vortex streets, then this proves that they interact with each other; even so, there might be no visual interaction between them downstream.

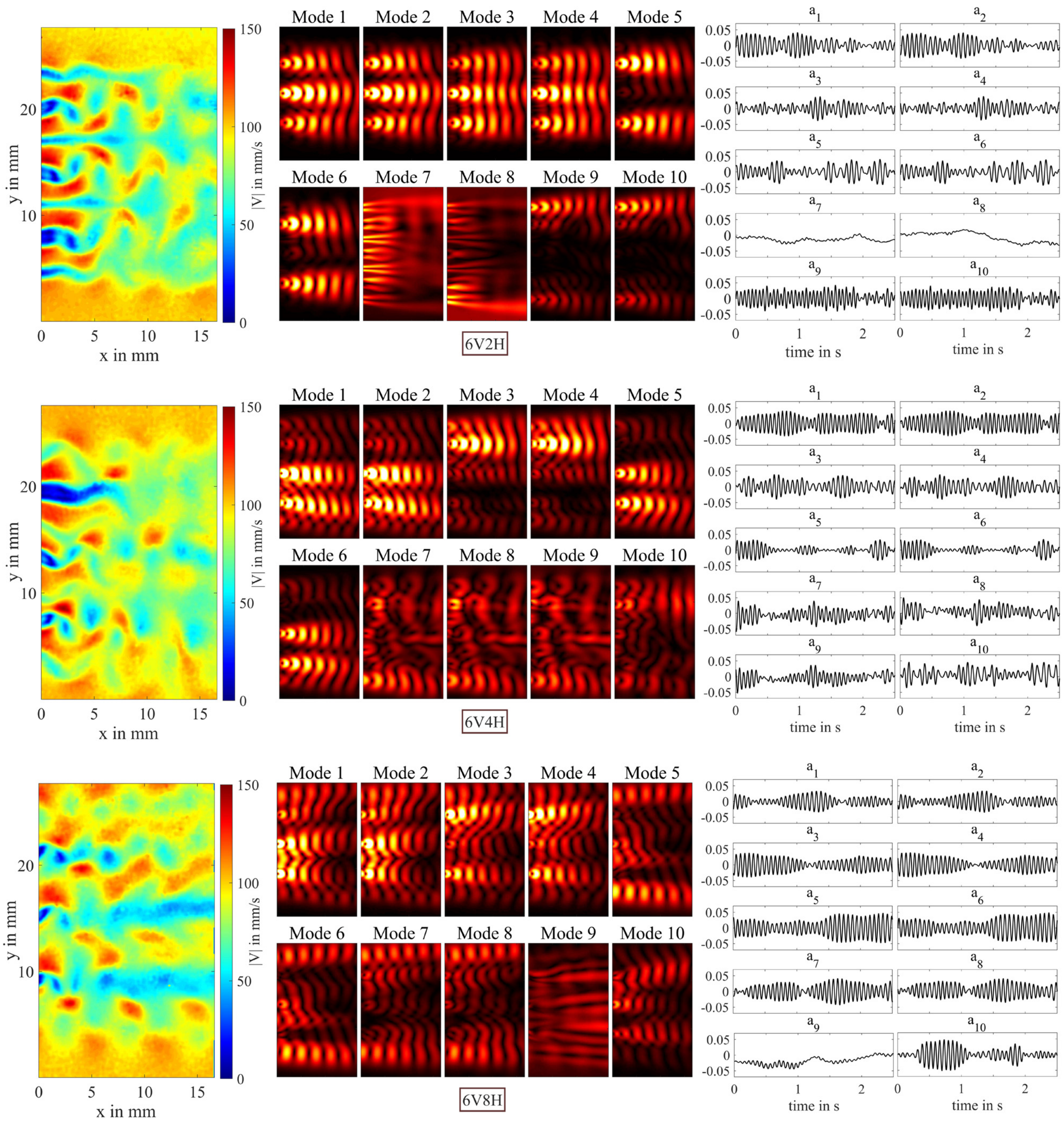

FIG. 10. The instantaneous absolute velocity field $|V|$ (left), the spatial POD modes (center), and their corresponding time coefficients (right) for the 6V2H, 6V4H, and 6V8H arrays at top, middle, and bottom, respectively.

The results for the 6V2H array are shown in Fig. 10, top. Here, the tails of the two central cylinders in the first column are stretched to the field of view and have separated the three vortex streets of the second column. Therefore, only the vortex streets of the upper and lower cylinders of the first and second columns collide with each other. Although the regular expectation is that these two pairs of vortex streets at the top and bottom might be synchronized with each other; however, this is not the case, and from the SPMs, it is evident that the three streets of the second column are strongly synchronized and have a frequency of 14 Hz. However, this synchronization appears in two main phases, the first two modes are for phase one, and the third and fourth modes are for phase two. The difference is whether the vortex centers of the central cylinder are in the same horizontal position as its two neighbors or not. The two cylinders at the edges of the first column oscillate with a higher frequency of 18 Hz. This might be the reason that they are unable to be synchronized with the other three vortex streets.

As H/D increase to 4 in 6V4H, all five vortex streets represent 19 Hz frequency. However, this does not result in fully synchronized vortex shedding in the flow. Based on the SPMs, it can be seen that the central vortex street is synchronized with the two lower streets, and the other two upper ones are synchronized together (see SPMs in Fig. 10 middle). The tail of the two central cylinders in the first column is now unable to separate the vortex streets, and they mix with the vortices themselves. Furthermore, from the larger recirculation zone for the upper cylinder in the second column in the instantaneous velocity field, it is apparent that while the time-averaged flow is symmetric, but asymmetries might happen in the individual time steps.

Finally, for 6V8H, the vortex shedding frequency for the five streets is reduced to 15 Hz. This is indeed interesting as one might assume that as the H/D increase from 4 to 8 the effect of the upstream column of the cylinders should be minimized, and thus, the vortex street must be further closer to the case of an isolated cylinder with the frequency of 22 Hz. Although the SPMs indicate some sort of synchronization between different vortex streets but seems that compared to previous cases, these synchronizations are further complex and change from time to time. Last but not least, due to the large horizontal distance, the tails of the two central cylinders in the first column have completely disappeared from the flow.

IV. CONCLUSIONS

In this study, experiments were conducted to study the flow dynamics and structure of nine arrays of multiple cylinders. Each array contained two columns of four (upstream) and three cylinders (downstream) in total. Nine different arrays were created by varying the distances between the columns and cylinders within each column for $V/D = 2$, 4, 6, and $H/D = 2$, 4, 8. PIV measurements were conducted for the arrays in a water channel at Re $\sim$100. In order to gain more insight into the flow dynamics, POD analysis was applied to the velocity fields. The main conclusions of the current study can be summed up as follows:

In contrast to a single cylinder in $Re = 100$, all arrays represented unsteady flow structures. This proves that the cylinders affect the flow behind each other as long as $V/D \leq 6$ and $H/D \leq 8$. Each array shows distinct features; thus, there might be even more flow regimes for intermediate distances. There are differences between the arrays in the number and shedding frequencies of the vortex streets, how they synchronize with neighboring streets, and whether the flow is symmetric or not.

The flow structures can be categorized into three general groups denoted as single bluff body, transitional, and co-shedding. A single bluff body flow with only large wake and thus one vortex street was observed for both 2V2H and 2V4H arrays, with the latter having stronger and more steady vortex shedding at similar frequency. Next are the 2V8H and 4V2H arrays, which deviate from single bluff body flow by representing individual vortex streets for the cylinders. However, the proximity of the cylinders results in an asymmetric flow, particularly for 4V2H. For the 4V8H array, the cylinder wakes in the second column have very distinct long tails. This suggests that when distances are carefully chosen, even in such large values of $V/D = 4$ and $H/D = 8$, vortex shedding behind cylinders can be suppressed. The remaining four arrays, namely, 4V4H, 6V2H, 6V4H, and 6V8H, all represent symmetric flows with five vortex streets belonging to the two upper and lower cylinders in the first column and the three in the second column. Other than the 6V2H array, whose cylinders in the second column show lower frequencies of vortex shedding, all other arrays have identical frequencies for all five vortex streets. For each array, however, the coupling of the phase of the vortex streets is distinct and different.

The current study reveals unique features of the flow behind cylinder arrays depending on their vertical and horizontal distances. This will have direct benefit in various applications to for example increase the heat transfer, lower the structural impact, avoid resonance, or provide maximum available vibrational energy for vortex-induced energy harvesting. There are however several possible directions that one can proceed to extend the topic. Minimal horizontal and vertical distance should be determined at which the effect of neighboring cylinders diminishes from the flow structure. This is especially important when numerous bodies (wind turbine supports, vortex-induced energy harvesters, skyscrapers, etc.) are to be distributed in a limited area without encountering the complications of wake interactions. Additionally, the maximum Reynolds number at which the steady flow structure appears must be determined. Depending on the distances, this may differ for each array. It will be interesting to measure the lift and drag loading over the cylinders on such arrays as well.

ACKNOWLEDGMENTS

This work is supported by the Carl Zeiss Foundation under the Project No. P 2018-02-001 "DeepTurb–Deep Learning in and of Turbulence." We thank Alexander Thieme, Chaitanya Tambe, and Adrian Unterseher for their valuable assistance in conducting the experiments.

AUTHOR DECLARATIONS

Conflict of Interest

The authors have no conflicts to disclose.

Author Contributions

Mohammad Sharifi Ghazijahani: Investigation (lead); Writing – original draft (lead). **Christian Cierpka:** Supervision (lead).

DATA AVAILABILITY

The data that support the findings of this study are available from the corresponding author upon reasonable request.

APPENDIX: A PROPER ORTHOGONAL DECOMPOSITION

Lumley[99] was the first to introduce proper orthogonal decomposition (POD) as a tool to visualize the hidden structures in the turbulent flow in fluid dynamics. Later, Sirovich[91] introduced the snapshot POD method in particular for the cases where discrete time steps of the flow are available experimentally or numerically. Assuming $u'(x,t)$ as the velocity fluctuations over time and space, POD transforms the u' to separate functions of time (t) and space (x)

$$u'(x,t) = \Sigma_{k=1}^{T} a_k(t)\Phi_k(x). \tag{A1}$$

Such that

$$\iiint_x \Phi_{k_1}(x)\Phi_{k_2}(x)\,dx = \begin{cases} 1 & \text{if } k_1 = k_2, \\ 0 & \text{if } k_1 \neq k_2. \end{cases} \tag{A2}$$

Here, the $\Phi_k(x)$ are the spatial modes and the $a_k(t)$ are their respective time coefficients. The spatial modes are deterministic and orthogonal to each other, whereas the time coefficients are random and solely dependent on their respective spatial mode. The motivation for data reduction via POD is that these deterministic spatial modes will reveal hidden structures in the turbulent flow, which are regularly unseen when velocity fields are observed. In this method, $\Phi_k(x)$ are the eigenvectors of the covariance matrix of the velocity, and their respective eigenvalue determines the ratio of the modal kinetic energy of the respective spatial mode to the total kinetic energy of the flow. Therefore, it is possible to determine, for instance, that how many percentages of total kinetic energy are captured by a limited number of the spatial modes. This is, in particular, useful when one aims to reduce the data to be used in machine learning for flow modeling.[94] For further detail about POD, see Ref. 100.

REFERENCES

[1] W. Hanke, M. Witte, L. Miersch, M. Brede, J. Oeffner, M. Michael, F. Hanke, A. Leder, and G. Dehnhardt, "Harbor seal vibrissa morphology suppresses vortex-induced vibrations," J. Exp. Biol. **213**, 2665–2672 (2010).

[2] H. R. Beem and M. S. Triantafyllou, "Wake-induced 'slaloming' response explains exquisite sensitivity of seal whisker-like sensors," J. Fluid Mech. **783**, 306–322 (2015).

[3] W.-L. Chen, X.-W. Min, and Y.-J. Guo, "Performance of seal vibrissa-inspired bionic surface in suppressing aerodynamic forces and vortex shedding around a circular cylinder," Ocean Eng. **260**, 112032 (2022).

[4] Y. J. Lee, Y. Qi, G. Zhou, and K. B. Lua, "Vortex-induced vibration wind energy harvesting by piezoelectric mems device in formation," Sci. Rep. **9**, 20404 (2019).

[5] B. Wilks, F. Montiel, and S. Wakes, "Rainbow reflection and broadband energy absorption of water waves by graded arrays of vertical barriers," J. Fluid Mech. **941**, A26 (2022).

[6] B. Zhang, Z. Mao, B. Song, W. Tian, and W. Ding, "Numerical investigation on VIV energy harvesting of four cylinders in close staggered formation," Ocean Eng. **165**, 55–68 (2018).

[7] Y.-F. Mei, C. Zheng, N. Aubry, M.-G. Li, W.-T. Wu, and X. Liu, "Active control for enhancing vortex induced vibration of a circular cylinder based on deep reinforcement learning," Phys. Fluids **33**, 103604 (2021).

[8] G. Sui, X. Shan, H. Tian, L. Wang, and T. Xie, "Study on different underwater energy harvester arrays based on flow-induced vibration," Mech. Syst. Signal Process. **167**, 108546 (2022).

[9] U. Latif, M. Y. Younis, S. Idrees, E. Uddin, A. Abdelkefi, A. Munir, and M. Zhao, "Synergistic analysis of wake effect of two cylinders on energy harvesting characteristics of piezoelectric flag," Renewable Sustainable Energy Rev. **173**, 113114 (2023).

[10] B. L. White and H. M. Nepf, "Scalar transport in random cylinder arrays at moderate Reynolds number," J. Fluid Mech. **487**, 43–79 (2003).

[11] D. D. Wangsawijaya, C. Nicolai, and B. Ganapathisubramani, "Time-averaged velocity and scalar fields of the flow over and around a group of cylinders: A model experiment for canopy flows," Flow **2**, E9 (2022).

[12] M. Liu, W. Huai, and B. Ji, "Characteristics of the flow structures through and around a submerged canopy patch," Phys. Fluids **33**, 035144 (2021).

[13] A. Gijón Mancheño, W. Jansen, J. C. Winterwerp, and W. S. Uijttewaal, "Predictive model of bulk drag coefficient for a nature-based structure exposed to currents," Nature **11**, 3517 (2021).

[14] C. Nicolai, S. Taddei, C. Manes, and B. Ganapathisubramani, "Wakes of wall-bounded turbulent flows past patches of circular cylinders," J. Fluid Mech. **892**, A37 (2020).

[15] W. Y. Chang, G. Constantinescu, and W. F. Tsai, "Effect of array submergence on flow and coherent structures through and around a circular array of rigid vertical cylinders," Phys. Fluids **32**, 035110 (2020).

[16] K. Chang, G. Constantinescu, and S. Park, "2-D eddy resolving simulations of flow past a circular array of cylindrical plant stems," J. Hydrodyn. **30**, 317–335 (2018).

[17] K. Kingora and H. Sadat, "Flow and scalar transfer characteristics for a circular colony of vegetation," Phys. Fluids **34**, 083606 (2022).

[18] J. Xu, L. Chen, D. Ning, and M. Zhao, "Resonance of water waves propagating over a uniform and a graded line array of rectified submerged cosinoidal bars," Appl. Ocean Res. **134**, 103531 (2023).

[19] K. Lam, J. Li, and R. So, "Force coefficients and Strouhal numbers of four cylinders in cross flow," J. Fluids Struct. **18**, 305–324 (2003).

[20] Z. Gui, Y. Shan, and C. Liu, "Flow velocity evolution through a floating rigid cylinder array under unidirectional flow," J. Hydrol. **617**, 128915 (2023).

[21] T. Tang, P. Yu, X. Shan, J. Li, and S. Yu, "On the transition behavior of laminar flow through and around a multi-cylinder array," Phys. Fluids **32**, 013601 (2020).

[22] J.-C. Lin, Y. Yang, and D. Rockwell, "Flow past two cylinders in tandem: Instantaneous and averaged flow structure," J. Fluids Struct. **16**, 1059–1071 (2002).

[23] Y. Zhou and M. Yiu, "Flow structure, momentum and heat transport in a two-tandem-cylinder wake," J. Fluid Mech. **548**, 17–48 (2006).

[24] S. R. Kumar, A. Sharma, and A. Agrawal, "Simulation of flow around a row of square cylinders," J. Fluid Mech. **606**, 369–397 (2008).

[25] N. Hosseini, M. Griffith, and J. Leontini, "Flow-induced vibrations in long rows of cylinders and their links to convective instabilities," Int. J. Heat Fluid Flow **94**, 108922 (2022).

[26] H. Eizadi, H. An, T. Zhou, H. Zhu, and L. Cheng, "Wake transitions of six tandem circular cylinders at low Reynolds numbers," Phys. Fluids **34**, 023605 (2022).

[27] V. D. Duong, V. D. Nguyen, V. T. Nguyen, and I. L. Ngo, "Low-Reynolds-number wake of three tandem elliptic cylinders," Phys. Fluids **34**, 043605 (2022).

[28] K. Kingora, M. M. Raza, and H. Sadat, "Flow and passive scalar transfer characteristics around a row of interacting tandem cylinders," J. Hydrodyn. **34**, 596–619 (2022).

[29] D. Kumar, K. Sourav, and S. Sen, "Steady separated flow around a pair of identical square cylinders in tandem array at low Reynolds numbers," Comput. Fluids **191**, 104244 (2019).

[30] H. H. Khan, M. Islam, Y. Y. Fatt, I. Janajreh, and M. M. Alam, "Effect of three tandem cylinder diameter difference on flow-induced vibrations and heat transfer," Int. J. Mech. Sci. **236**, 107764 (2022).

[31] F. Freidooni, A. Sohankar, M. Rastan, and E. Shirani, "Flow field around two tandem non-identical-height square buildings via LES," Build. Environ. **201**, 107985 (2021).

[32] E. E. Essel, R. Balachandar, and M. F. Tachie, "Effects of sheltering on the unsteady wake dynamics of tandem cylinders mounted in a turbulent boundary layer," J. Fluid Mech. **954**, A40 (2023).

[33] X. Xu, S. Yi, P. Quan, H. Xiong, and L. Nie, "Experimental study on the hypersonic boundary layer transition induced by tandem cylinders," Exp. Therm. Fluid Sci. **145**, 110901 (2023).

[34] M. Rastan and M. M. Alam, "Transition of wake flows past two circular or square cylinders in tandem," Phys. Fluids **33**, 081705 (2021).

[35] H. Zhang, L. Zhou, and K. Tim, "Mode-based energy transfer analysis of flow-induced vibration of two rigidly coupled tandem cylinders," Int. J. Mech. Sci. **228**, 107468 (2022).
[36] H. H. Khan, M. D. Islam, Y. Y. Fatt, I. Janajreh, and M. M. Alam, "Flow-induced vibration on two tandem cylinders of different diameters and spacing ratios," Ocean Eng. **258**, 111747 (2022).
[37] Q. Zhou, M. M. Alam, S. Cao, H. Liao, and M. Li, "Numerical study of wake and aerodynamic forces on two tandem circular cylinders at $Re = 10^3$," Phys. Fluids **31**, 045103 (2019).
[38] L. Zhou, H. Li, K. Tim, X. He, G. Y. C. Maceda, and H. Zhang, "Sensitivity-aided active control of flow past twin cylinders," Int. J. Mech. Sci. **242**, 108013 (2023).
[39] W. Gu, X. Xu, M. Jiang, and W. Yao, "Effects of spacing ratio on vortex-induced vibration of twin tandem diamond cylinders in a steady flow," Phys. Fluids **35**, 043604 (2023).
[40] D. Kumar and K. Sourav, "Vortex-induced vibrations of tandem diamond cylinders: A novel lock-in behavior," Int. J. Mech. Sci. **255**, 108463 (2023).
[41] J. F. Derakhshandeh and M. M. Alam, "Reynolds number effect on the flow past two tandem cylinders," Wind Struct. **30**, 475 (2020).
[42] J. F. Derakhshandeh, Y. Gharbia, and C. Ji, "Numerical investigations on flow over tandem grooved cylinders," Ocean Eng. **251**, 111160 (2022).
[43] W. Xu, C. Ji, H. Sun, W. Ding, and M. M. Bernitsas, "Flow-induced vibration of two elastically mounted tandem cylinders in cross-flow at subcritical Reynolds numbers," Ocean Eng. **173**, 375–387 (2019).
[44] N. B. Darbhamulla and R. Bhardwaj, "Flow-induced vibrations of circular cylinder in tandem arrangement with D-section cylinder at low Reynolds number," Phys. Fluids **33**, 053606 (2021).
[45] W. Stankiewicz, "Recursive dynamic mode decomposition for the flow around two square cylinders in tandem configuration," J. Fluids Struct. **110**, 103515 (2022).
[46] M. Zdravkovich, "The effects of interference between circular cylinders in cross flow," J. Fluids Struct. **1**, 239–261 (1987).
[47] N. Hosseini, M. D. Griffith, and J. S. Leontini, "Flow states and transitions in flows past arrays of tandem cylinders," J. Fluid Mech. **910**, A34 (2021).
[48] D. Guillaume and J. LaRue, "Investigation of the flopping regime with two-, three-and four-cylinder arrays," Exp. Fluids **27**, 145–156 (1999).
[49] H. Akilli, A. Akar, and C. Karakus, "Flow characteristics of circular cylinders arranged side-by-side in shallow water," Flow Meas. Instrum. **15**, 187–197 (2004).
[50] Z. Huang, J. Olson, R. Kerekes, and S. Green, "Numerical simulation of the flow around rows of cylinders," Comput. Fluids **35**, 485–491 (2006).
[51] A. Agrawal, L. Djenidi, and R. Antonia, "Investigation of flow around a pair of side-by-side square cylinders using the lattice Boltzmann method," Comput. Fluids **35**, 1093–1107 (2006).
[52] L. Kun, D.-J. Sun, X.-Y. Yin *et al.*, "Wake patterns of flow past a pair of circular cylinders in side-by-side arrangements at low Reynolds numbers," J. Hydrodyn., Ser. B **19**, 690–697 (2007).
[53] D. Chatterjee, G. Biswas, and S. Amiroudine, "Numerical simulation of flow past row of square cylinders for various separation ratios," Comput. Fluids **39**, 49–59 (2010).
[54] P. Burattini and A. Agrawal, "Wake interaction between two side-by-side square cylinders in channel flow," Comput. Fluids **77**, 134–142 (2013).
[55] Y. Yan, C. Ji, and N. Srinil, "Three-dimensional flip-flopping flow around a pair of dual-stepped circular cylinders in a side-by-side arrangement," Phys. Fluids **32**, 123608 (2020).
[56] Y. Yan, C. Ji, and N. Srinil, "On wake modulation and interaction features of a pair of dual-step circular cylinders in side-by-side arrangements," Phys. Fluids **33**, 093604 (2021).
[57] K. Kingora, W. L. Burks, and H. Sadat, "Flow and mass transfer characteristics for interacting side-by-side cylinders," Phys. Fluids **34**, 023602 (2022).
[58] S. Tao and Y. Zhou, "Turbulent flows around side-by-side cylinders with regular and multiscale arrangements," Phys. Rev. Fluids **4**, 124602 (2019).
[59] P. Sooraj, M. H. Khan, A. Sharma, and A. Agrawal, "Wake analysis and regimes for flow around three side-by-side cylinders," Exp. Therm. Fluid Sci. **104**, 76–88 (2019).
[60] P. Baj and O. R. Buxton, "Passive scalar dispersion in the near wake of a multi-scale array of rectangular cylinders," J. Fluid Mech. **864**, 181–220 (2019).
[61] W. Chen, C. Ji, N. Srinil, Y. Yan, and Z. Zhang, "Effects of upstream wake on vortex-induced vibrations and wake patterns of side-by-side circular cylinders," Mar. Struct. **84**, 103223 (2022).
[62] W. Chen, C. Ji, M. M. Alam, and Y. Yan, "Three-dimensional flow past two stationary side-by-side circular cylinders," Ocean Eng. **244**, 110379 (2022).
[63] W. Xu, S. Zhang, Y. Ma, and B. Liu, "Fluid forces acting on three and four long side-by-side flexible cylinders undergoing flow-induced vibration (FIV)," Mar. Struct. **75**, 102877 (2021).
[64] N. Krishna Chaitanya and D. Chatterjee, "Mixed convective flow past counter-rotating side-by-side cylinders at low Reynolds number," Numer. Heat Transfer, Part A **83**, 141–159 (2023).
[65] L. Li, Z. Yan, and Z. Pan, "Vortex-induced rotations of two side-by-side square cylinders in a two-dimensional microchannel," Phys. Fluids **33**, 117104 (2021).
[66] S. Kang, "Numerical study on laminar flow over three side-by-side cylinders," KSME Int. J. **18**, 1869–1879 (2004).
[67] Z. Han, D. Zhou, and J. Tu, "Laminar flow patterns around three side-by-side arranged circular cylinders using semi-implicit three-step Taylor-characteristic-based-split (3-TCBS) algorithm," Eng. Appl. Comput. Fluid Mech. **7**, 1–12 (2013).
[68] M. Akbari and S. Price, "Numerical investigation of flow patterns for staggered cylinder pairs in cross-flow," J. Fluids Struct. **20**, 533–554 (2005).
[69] M. M. Alam and H. Sakamoto, "Investigation of Strouhal frequencies of two staggered bluff bodies and detection of multistable flow by wavelets," J. Fluids Struct. **20**, 425–449 (2005).
[70] M. M. Alam and J. P. Meyer, "Global aerodynamic instability of twin cylinders in cross flow," J. Fluids Struct. **41**, 135–145 (2013).
[71] F. Tong, L. Cheng, and M. Zhao, "Numerical simulations of steady flow past two cylinders in staggered arrangements," J. Fluid Mech. **765**, 114–149 (2015).
[72] R. Wang, Y. He, L. Chen, Y. Zhu, and Y. Wei, "Numerical simulations of flow around three cylinders using momentum exchange-based immersed boundary-lattice Boltzmann method," Ocean Eng. **247**, 110706 (2022).
[73] S. Yang, W. Yan, J. Wu, C. Tu, and D. Luo, "Numerical investigation of vortex suppression regions for three staggered circular cylinders," Eur. J. Mech.-B **55**, 207–214 (2016).
[74] A. V. de Paula, L. A. M. Endres, and S. V. Möller, "Experimental study of the bistability in the wake behind three cylinders in triangular arrangement," J. Braz. Soc. Mech. Sci. Eng. **35**, 163–176 (2013).
[75] S. Zheng, W. Zhang, and X. Lv, "Numerical simulation of cross-flow around three equal diameter cylinders in an equilateral-triangular configuration at low Reynolds numbers," Comput. Fluids **130**, 94–108 (2016).
[76] M. Bansal and S. Yarusevych, "Experimental study of flow through a cluster of three equally spaced cylinders," Exp. Therm. Fluid Sci. **80**, 203–217 (2017).
[77] R. Wang, B. Lu, X. Zuo, L. Yan, Y. Zhu, and Y. Wei, "Numerical computations of flow around three equilateral-triangular square cylinders with rounded corners using momentum exchange-based IB-LBM at low Reynolds numbers," Ocean Eng. **263**, 112373 (2022).
[78] M. Zhang, B. Yin, D. Guo, Z. Ji, and G. Yang, "Numerical study on the flow past three cylinders in equilateral-triangular arrangement at $Re = 3 \times 10^6$," Appl. Sci. **12**, 11835 (2022).
[79] W. Chen, C. Ji, M. M. Alam, J. Williams, and D. Xu, "Numerical simulations of flow past three circular cylinders in equilateral-triangular arrangements," J. Fluid Mech. **891**, A14 (2020).
[80] W. Chen, C. Ji, D. Xu, and Z. Zhang, "Oscillation regimes and mechanisms in the vortex-induced vibrations of three circular cylinders with equilateral-triangular arrangements," Phys. Fluids **32**, 043602 (2020).
[81] Y. Gao, W. Chen, B. Wang, and L. Wang, "Numerical simulation of the flow past six-circular cylinders in rectangular configurations," J. Mar. Sci. Technol. **25**, 718–742 (2020).
[82] G. Y. Cornejo Maceda, Y. Li, F. Lusseyran, M. Morzyński, and B. R. Noack, "Stabilization of the fluidic pinball with gradient-enriched machine learning control," J. Fluid Mech. **917**, A42 (2021).

[83]N. Deng, B. R. Noack, M. Morzyński, and L. R. Pastur, "Galerkin force model for transient and post-transient dynamics of the fluidic pinball," J. Fluid Mech. **918**, A4 (2021).
[84]N. Deng, B. R. Noack, M. Morzyński, and L. R. Pastur, "Cluster-based hierarchical network model of the fluidic pinball—Cartographing transient and post-transient, multi-frequency, multi-attractor behaviour," J. Fluid Mech. **934**, A24 (2022).
[85]Y. Li, W. Cui, Q. Jia, Q. Li, Z. Yang, M. Morzyński, and B. R. Noack, "Explorative gradient method for active drag reduction of the fluidic pinball and slanted Ahmed body," J. Fluid Mech. **932**, A7 (2022).
[86]M. Raffel, C. E. Willert, J. Kompenhans *et al.*, *Particle Image Velocimetry: A Practical Guide* (Springer, 1998), Vol. 2.
[87]J. Westerweel, "Fundamentals of digital particle image velocimetry," Meas. Sci. Technol. **8**, 1379 (1997).
[88]J. Westerweel and F. Scarano, "Universal outlier detection for PIV data," Exp. Fluids **39**, 1096–1100 (2005).
[89]C. J. Kähler, S. Scharnowski, and C. Cierpka, "On the resolution limit of digital particle image velocimetry," Exp. Fluids **52**, 1629–1639 (2012).
[90]C. J. Kähler, T. Astarita, P. P. Vlachos, J. Sakakibara, R. Hain, S. Discetti, R. La Foy, and C. Cierpka, "Main results of the 4th international PIV challenge," Exp. Fluids **57**, 97 (2016).
[91]L. Sirovich, "Turbulence and the dynamics of coherent structures. I. Coherent structures," Q. Appl. Math. **45**, 561–571 (1987).
[92]A. Deane, I. Kevrekidis, G. E. Karniadakis, and S. Orszag, "Low-dimensional models for complex geometry flows: Application to grooved channels and circular cylinders," Phys. Fluids A **3**, 2337–2354 (1991).
[93]C. Cierpka, T. Weier, and G. Gerbeth, "Synchronized force and particle image velocimetry measurements on a NACA 0015 in poststall under control of time periodic electromagnetic forcing," Phys. Fluids **22**, 075109 (2010).
[94]M. S. Ghazijahani, F. Heyder, J. Schumacher, and C. Cierpka, "On the benefits and limitations of echo state networks for turbulent flow prediction," Meas. Sci. Technol. **34**, 014002 (2023).
[95]N. Hosseini, M. D. Griffith, and J. S. Leontini, "The flow past large numbers of cylinders in tandem," J. Fluids Struct. **98**, 103103 (2020).
[96]A. Fishman, J. M. Rossiter, J. S. Leontini, and M. E. Homer, "Mixing in arrays of villi-like actuators," Phys. Fluids **34**, 094112 (2022).
[97]P. J. Kristo and M. L. Kimber, "Cylinders and jets in crossflow: Wake formations as a result of varying geometric proximities," Phys. Fluids **33**, 055106 (2021).
[98]X. Sun, S. Suh, Z.-H. Ye, and Y.-X. Zhang, "Sub-harmonic wake-induced vibration of five tandem circular cylinders at low Reynolds number of 100," Theor. Comput. Fluid Dyn. **36**, 671–687 (2022).
[99]J. L. Lumley, "The structure of inhomogeneous turbulent flows," Atmos. Turbul. Radio Wave Propag. **1967**, 166–178.
[100]J. Weiss, "A tutorial on the proper orthogonal decomposition," AIAA Paper No. 2019-3333, 2019.